ICARUS 103, 215–234 (1993)

The Occultation of 28 Sgr by Saturn: Saturn Pole Position and Astrometry

W. B. HUBBARD,[1,2] C. C. PORCO,[1,2] D. M. HUNTEN,[1] G. H. RIEKE,[1,3] M. J. RIEKE,[3] D. W. MCCARTHY,[3] V. HAEMMERLE,[1] R. CLARK,[1] E. P. TURTLE,[1] J. HALLER,[3] B. MCLEOD,[3] L. A. LEBOFSKY,[1] R. MARCIALIS,[1] AND J. B. HOLBERG[1]

University of Arizona, Tucson, Arizona 85721

R. LANDAU[4] AND L. CARRASCO

Observatorio Astronómico de San Pedro Mártir, 22860 Ensenada, B. C., México

J. ELIAS

Cerro Tololo Interamerican Observatory, Casilla 603, La Serena, Chile 1353

M. W. BUIE

Lowell Observatory, Flagstaff, Arizona 86001

S. E. PERSSON, T. BOROSON, AND S. WEST

Mount Wilson and Las Campanas Observatories, 813 Santa Barbara Street, Pasadena, California 91101

AND

D. J. MINK

Harvard–Smithsonian Center for Astrophysics, 60 Garden Street, Cambridge, Massachusetts 02138

Received August 31, 1992; revised March 1, 1993

We determine the geometry of the 3 July 1989 occultation of 28 Sgr by Saturn and use the results to derive Saturn's pole as defined by the ring plane. The analysis makes use of high-precision timings of 12 circular edges in the C-ring (radii = 84750 to 90615 km), three features in the Cassini division, the edges of the Encke gap, and the outer edge of the Keeler gap. Our group of observing sites includes one southern hemisphere station (CTIO) and five northern hemisphere stations (three Tucson-area stations, the UK Infrared Telescope in Hawaii, and San Pedro Mártir in Baja California), which provides a terrestrial chord separation ~10,000 km. Assuming ring radii obtained from an analysis of *Voyager* radio- and stellar-occultation data (P. D. Nicholson, M. L. Cooke, and E. Pelton, 1990, *Astron. J.* **100**, 1339–1362), we use edge timings to solve for the position angle and opening angle of the apparent ring ellipses. The star 28 Sgr appears to be well represented as a uniformly illuminated disk with an apparent radius of 9.0 ± 0.3 km projected at Saturn at the wavelengths of observation ($\lambda \sim 3$ μm). The internal consistency of the data set and redundancy of stations indicates that the relative positional error of a given sharp ring edge timing is at the level of 2 km or smaller; the absolute error is roughly 5 km. Our derived pole position, $\alpha_p = 40.599° \pm 0.020°$, $\delta_p = 83.536° \pm 0.005°$, is consistent with the pole and ring radius scale deduced from *Voyager* stellar and radio occultation observations (P. D. Nicholson, M. L. Cooke, and E. Pelton, 1990, *Astron. J.* **100**, 1339–1362) and the solution found in the accompanying paper (French *et al.*, 1993, this issue).

1. INTRODUCTION

The occultation of the bright star 28 Sgr (V = 5.37, B-V = 1.64, spectral class K4III) by Saturn, its rings, and Titan on 3 July 1989 was observed by many professional and amateur astronomers from the eastern and western

[1] Lunar and Planetary Laboratory.

[2] Visiting Astronomer, Cerro Tololo Inter-American Observatory, National Optical Astronomy Observatories, operated by the Association of Universities for Research in Astronomy, Inc., under contract with the National Science Foundation.

[3] Steward Observatory.

[4] Present address: Australia Telescope, Box 94, Narrabri NSW 2390, Australia.

0019-1035/93 $5.00

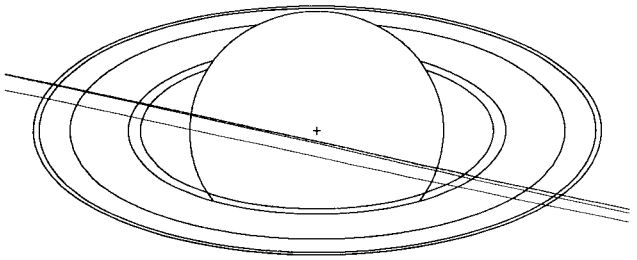

FIG. 1. Overall view of the geometry of the 28 Sgr occultation, together with station chords which provided data for our solution. The southern chord, CTIO, is well separated from the others and plays a crucial role in the analysis. Points on the chords move from right to left (west to east) as time increases. The ring radii shown correspond to those listed in Table I: the outermost feature is the Keeler gap, next the Encke division, then a ring corresponding to the general radius of the three Cassini divisions, and finally, two rings which denote the innermost and outermost of the C ring edges used.

tion is obtained through the use of the Cassini-division and A-ring features. The straight lines in Fig. 1 show the paths of all of the stations whose timings were used in this analysis. Figure 2 shows these paths in higher resolution west of the planetary limb. As in Fig. 1, the y-axis in Fig. 2 is oriented along the projection of Saturn's spin axis in the sky plane. In Figs. 1 and 2, paths of our stations are plotted with solid lines, whereas those of NE are plotted with dashed lines. The latter are for the most part invisible on this scale as they overlap substantially with our North American stations except for Hawaii. In Hawaii, our UKIRT experiment and NE's IRTF experiment were at adjacent telescopes on Mauna Kea.

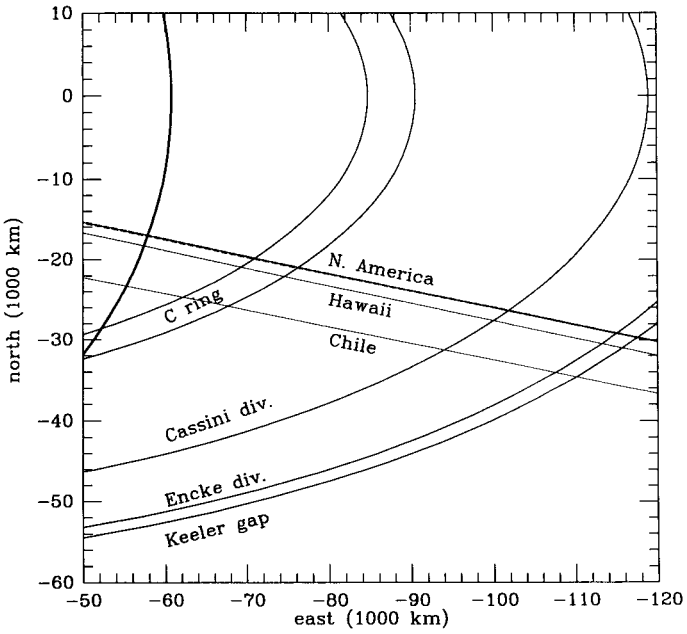

FIG. 2. Expanded view of the immersion limb in Fig. 1.

This paper is organized as follows. In Section 2 we describe the six experiments and the methods of data reduction, including a discussion of methods used to reduce noise and otherwise smooth the data. Section 3 discusses the method of using atmospheric scintillations to independently calibrate timings at different stations. Section 4 discusses the fiducial features and presents a table of timings. Section 5 presents the method used to reduce the timings, and the results for Saturn's pole position and ring radius scale. We conclude with a discussion in Section 6.

2. DESCRIPTION OF EXPERIMENTS

Table II lists the relevant parameters for the six experiments used in determining the Saturn pole and ring radius scale. The 28 Sgr data are classifiable into data from (1) aperture experiments, in which the stellar flux within a fixed aperture is continuously measured, and (2) array experiments, in which the star and occulting planet are rapidly imaged on a two-dimensional array. The advantage of experiments of type (1) is that variations in the flux can be measured at a high frequency, typically about 10 Hz, and the data set is more accessible to immediate reduction as it consists of a simple table of flux vs time. The disadvantage of (1) is that a spatially varying ring background signal is also measured in the aperture and cannot be straightforwardly removed. The advantage of (2) is that it provides a precise separate measurement of the background signal at all times. The disadvantages of (2) are that the data take longer to reduce, and the data rate is substantially lower, typically around 2 Hz. In this paper we are concerned with the precise location of sharp ring edges; the determination of a slowly varying background signal is of minor concern.

During aperture observations of the ring occultation, the aperture was centered on the star at all times. An accurate prediction ephemeris for each station was available for this purpose (D. J. Mink, personal communication, 1989) and was needed during the times when the star essentially vanished behind the B-ring. During the period of planetary occultation, the observers attempted to follow the predicted position of the primary refracted image along the southern limb of Saturn, but after the stellar flux had diminished substantially this strategy was difficult to implement. In general, guiding errors were infrequent and affected only a few of the events analyzed in this paper. All stations experienced photometric conditions throughout the occultation.

Figures 3a–3f provide a convenient overview of the data set used in this analysis. These figures plot the approximate optical depth as a function of ring-plane radius at each station for both the inbound (ingress) and outbound (egress) part of the ring occultation. Panels are

hemispheres. The combined data set is capable of yielding very high-precision information on the structure of Saturn's rings (Turtle *et al.* 1990, 1991), its atmosphere, and its largest satellite Titan (Hubbard *et al.* 1990a, 1993, Sicardy *et al.* 1990). The relative positions of the observing telescopes in the shadow plane are known with precisions on the order of tens of meters, but the absolute position of the center of the shadow and the precise aspect of the ring system projected in the shadow are less well known and are best determined from the data set itself. Determination of the exact occultation geometry is also essential to a detailed analysis of ring and atmospheric structure.

This paper carries out an essential first step in the analysis of 28 Sgr data by employing a subset of these data to provide the necessary calibration of the geometry for further analysis. We are concerned with the determination of the locations of 12 sharp-edged features in the C ring, 3 features in the Cassini division, the edges of the Encke gap, and the outer edge of the Keeler gap, all of which exhibit radial variations in Voyager imaging and occultation data of $\leq \pm 2$ km. The features are characterized by sharp, virtually discontinuous changes in optical depth as a function of radius and thus can be considered in this data set as semitransparent knife edges which sweep across the finite projected disk of 28 Sgr. Although the star has a projected diameter of 18 km at Saturn, the unocculted stellar profile appears to be well approximated by a uniformly illuminated disk. Thus the instant that a knife edge passes over the centroid of the projected stellar disk can be located to a spatial precision of ~1 km, which is comparable to the precision of the best *Voyager*-based data.

At the 1-km level of precision, many effects must be taken into consideration in solving for the ring geometry. The large angular size of the Saturn ring system (over 40 arcsec) and the precision of the data set combine to produce an unprecedented challenge to standard methods for the reduction of ground-based stellar occultation data. Previously developed astrometric algorithms, which we have applied to observations of occultations by Neptune and other bodies (e.g., Hubbard *et al.* 1987), do not suffice for the Saturn data set.

Our basic objective is to find a solution that is compatible with the most recent analysis of the *Voyager* radio and stellar occultation data (Nicholson *et al.* 1990; NCP hereafter), and which is fully consistent among all 28 Sgr occultation data sets of comparable precision. In order to accomplish this goal, timings of a set of fiducial ring features were exchanged with observers of the 28 Sgr occultation at stations other than our own (French *et al.* 1993). In the following, we refer to the companion paper by French *et al.* and the corresponding authors as the northeast group, or NE. The present paper is authored by the southwest (SW) group.

A common set of pooled ring edge timings from 10 stations distributed over 5 geographically diverse locations has been used in independent reduction and analysis schemes by the NE and SW groups. The timings were obtained independently by each group from its own proprietary data and then contributed to the pool. The methods adopted for the data reductions and the algorithms used in determining the astrometry were entirely independent. In general, the two analyses were kept as independent as possible, with the following exceptions: Certain standard solutions were compared at intermediate stages, which proved useful in exposing inadequate approximations as well as systematic timing problems at certain stations. Timing calibrations between our stations and those of NE were achieved by making use of cross-correlations of scintillations of 28 Sgr in Saturn's atmosphere, as described below. This process has led to the satisfactory result that the independent but concordant final solutions for the 28 Sgr-based ring radius scale and Saturn pole position are in agreement with the results of NCP.

The fiducial features adopted in this analysis are listed in Table I, together with the radius R of the feature from the center of Saturn as determined by NCP. Our numbering system for these features is arbitrary, and we list the corresponding number for each feature used by NE; the latter is in most cases consistent with the numbering of NCP.

Figure 1 illustrates the general geometry of the Saturn occultation. Although most of the fiducial features lie in the C-ring, substantial leverage on the astrometric solu-

TABLE I
Fiducial Ring Features

ring (this paper)	ring (NE)	comments	R_{NCP} (km)
1	23	C-ring feature	90615.163
2	24	C-ring feature	90404.558
3	25	C-ring feature	89939.913
4	26	C-ring feature	89787.932
5	41	C-ring feature	89296.271
6	27	C-ring feature	89189.284
7	28	C-ring feature	88595.116
8	29	C-ring feature	86603.073
9	30	C-ring feature	86370.762
10	42	C-ring feature	85759.659
11	34	C-ring feature	84950.453
12	35	C-ring feature	84749.859
14	1	Keeler gap outer edge	136521.668
16	3	Encke div. outer edge	133745.499
17	4	Encke div. inner edge	133424.226
19	7	Cassini div. feature	122047.573
20	15	Cassini div. feature	118965.036
21	13	Cassini div. feature	118627.166

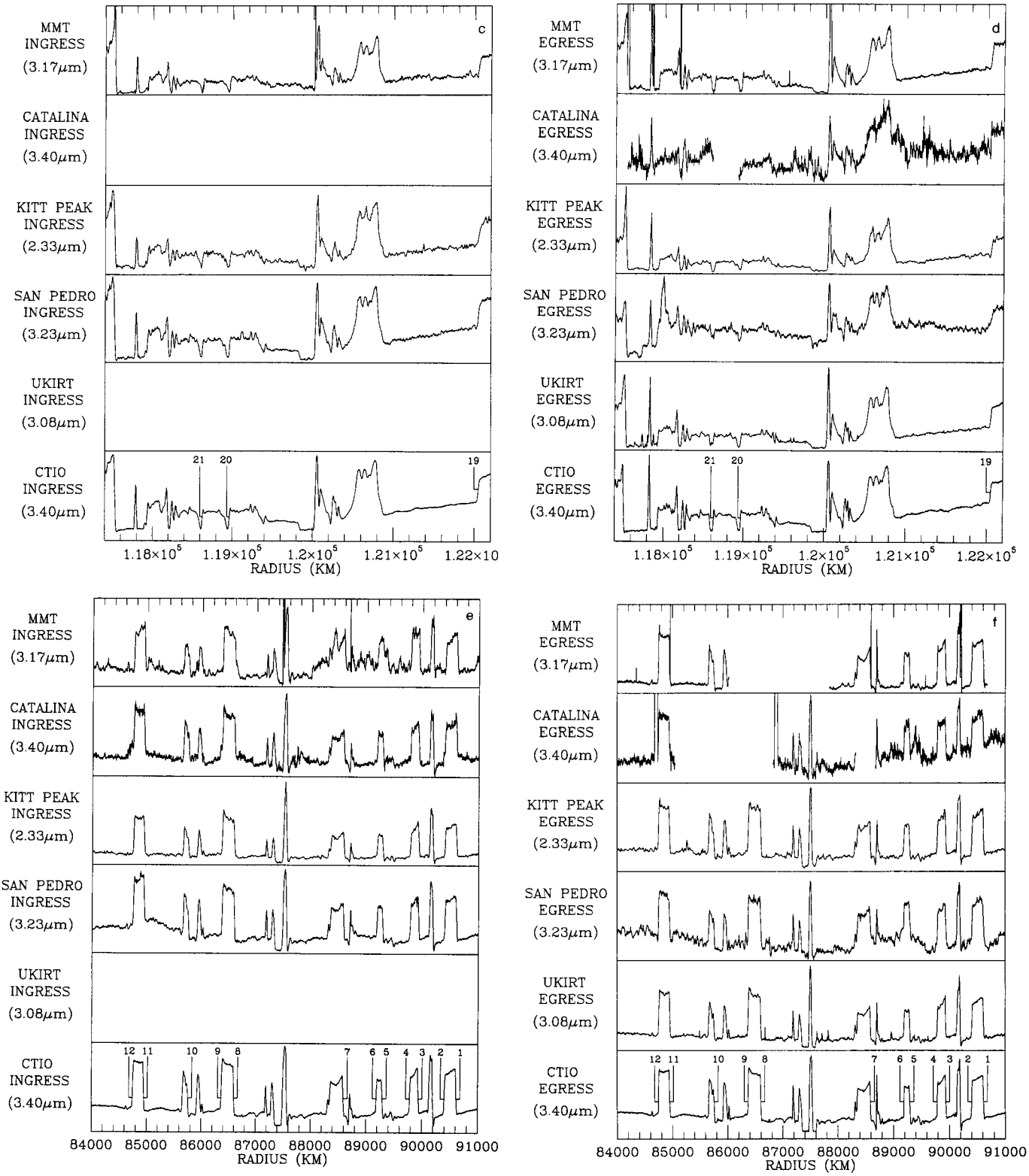

FIG. 3—*Continued*

TABLE II
Station Parameters

Sta.	Location	Telescope	$\Delta\lambda/\lambda$ (μm)	Scale	Sampling (Hz)	Latitude	Longitude	Elev. (m)
1	Mt. Hopkins	MMT	0.04/3.17	8″	10	31° 41′ 19.6″	110° 53′ 4.3″ W	2608
2	Catalina Sta.	1.54 m	0.20/3.40	8″	10	32° 25′ 0.7″	110° 43′ 55.1″ W	2510
3	(SO) Kitt Peak	2.3 m	0.07/2.33	0.58″/pix	2	31° 57′ 47.0″	111° 35′ 57.8″ W	2076
4	San Pedro Mártir	2.1 m	0.10/3.23	7″	10	31° 2′ 38.0″	115° 27′ 47.0″ W	2830
5	UKIRT	3.8 m	0.08/2.3; 0.03/3.08	0.6″/pix	3	19° 49′ 32″	155° 28′ 23″ W	4198
7	Cerro Tololo	4 m	0.07/3.40	8″	50	−30° 9′ 57.8″	70° 48′ 53.6″ W	2235

blank where data are missing, as is explained in the following discussion. At CTIO, the innermost part of the C-ring (not shown in Fig. 3e) was obscured by Saturn's atmosphere during immersion, at about 6:50 UTC; interference between the atmosphere and C-ring did not occur at the northern hemisphere stations.

2.1. Aperture Experiments

2.1.1. Mt. Hopkins MMT and Catalina Station 1.54 m. The two experiments in southern Arizona at the Multiple Mirror Telescope (MMT) and at Catalina Station (1.54 m) both made use of 8-arcsec apertures, 10-Hz chopping frequencies, and identical data-logging systems; both suffered from problems in the signal chain and in the absolute timing calibration. The MMT observed with an infrared photometer at a wavelength of 3.17 μm and a passband of 0.04 μm; the 1.54 m, with an infrared photometer at a wavelength of 3.40 μm and a passband of 0.20 μm. The raw data recorded during these aperture experiments consisted of a change in voltage measured during the course of a 0.1-sec chopper cycle from star to sky and back to star. A bias voltage was imposed on this

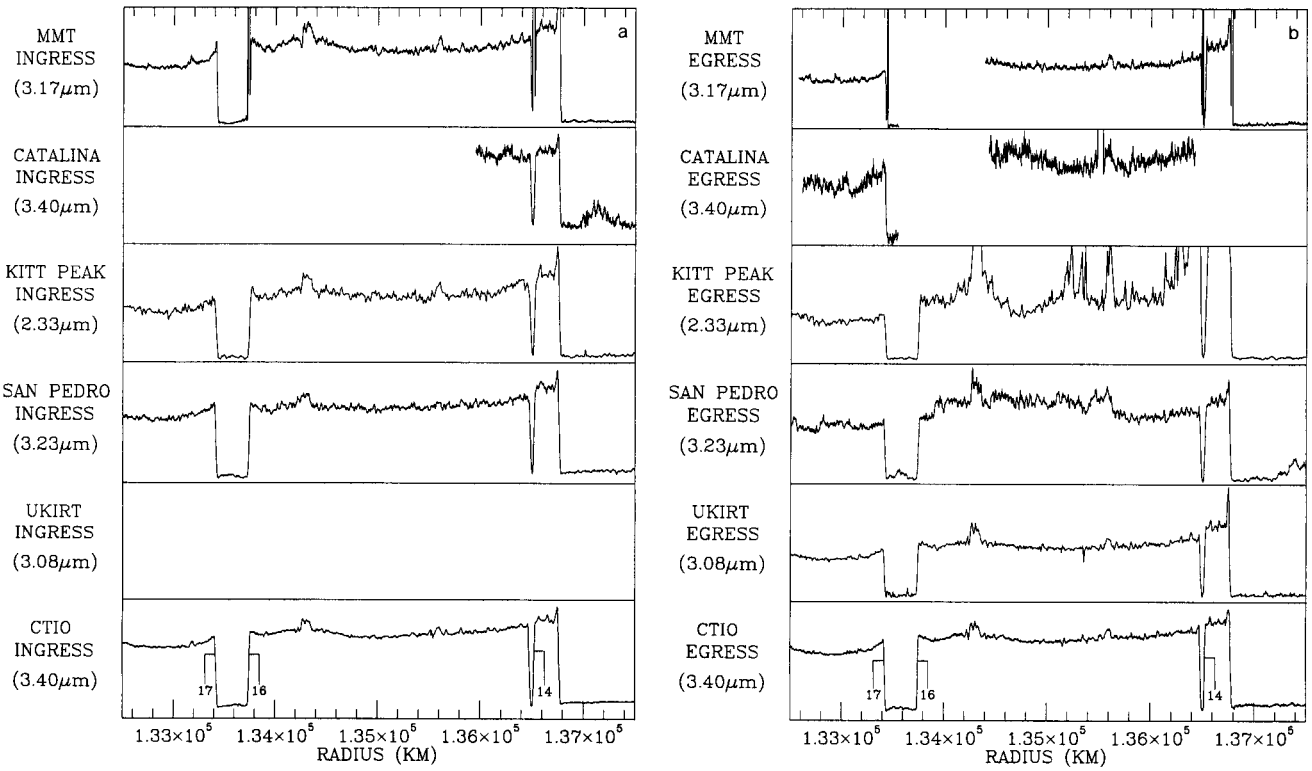

FIG. 3. Optical depth (unlabeled ordinate) vs ring plane radius for data acquired at 6 stations of the SW group. Plots show the ring regions—the outer A-ring (a, b), the Cassini division (c, d), and the outer C-ring (e, f)—seen in ingress and egress and within which sharp-edged fiducial features were chosen for this study. The fiducial features, labeled in accordance with Table I, are indicated in the CTIO plots. Some plots are blank, or partially blank, because of missing data (see text). The "overshooting" events seen associated with some sharp-edged features in the MMT data set are caused by problems discussed in the text. A variable background level and seeing disturbances caused the Kitt Peak egress data for the outer A-ring to exhibit a low spatial frequency variation in optical depth. Consequently, the data were scaled so that the depth of the Encke gap roughly matched that seen in the other data sets.

throughout the observations. The time delays introduced by the lock-in amplifier were <50 msec and stable. The response of the system to an applied square-wave signal was measured and showed an exponential time constant of 110 msec.

The occultation was monitored visually using an ISIT TV camera viewing the same field as the photometer through a dichroic. Guiding was accomplished during most of the event using the 4-m telescope's offset guider. The exceptions to this were 15-min periods after immersion and before emersion, when the telescope was guided on the predicted position of the primary refracted image of 28 Sgr. Data were recorded continuously from 4:18 UTC, roughly 2 hr before ring system immersion, until 10:20 UTC, about 1 hr after ring system emersion. The overall quality of the data was good, except for the last 45 min, when the seeing began to degrade seriously due to the increasing airmass of the object, producing signal variations.

The amplifier's 50-Hz sampling of the 18-Hz preamp output showed up as a strong 13.37-Hz signal superimposed on the data. Power spectra were computed for several samples of the data and other (weaker) heterodynes produced by this modulation were found at 18.31 and 23.26 Hz. Another minor set of semipermanent spectral features was found at lower integral frequencies, usually becoming noticeable against the background at either 2 or 3 Hz. (No 1-Hz component could be detected above the background.) This proved to be signal leakage from the timing signals being recorded on a second data channel as a 100-msec pulse every second. Two additional unexplained features remained in the power spectra of some parts of the data; e.g., a very sharp feature was present at 9.88 Hz in some regions (e.g., C ring) but was totally absent in most regions. The other feature, an associated pair of small peaks at 5.1 and 8.4 Hz, was present in some of the denser regions such as the A and B rings but was absent in the C ring. It was also absent when the star was behind the planet. These latter features were very small in magnitude and were not filtered from the final data set.

A low-pass spectral filter, utilizing notch filters centered at the spikes caused by the clock coupling and built to suppress all frequencies higher than the low frequency wing of the 13-Hz spike, was ultimately applied to the data. The resulting filtered CTIO data are among the highest quality data sets at our disposal.

2.2. Array Experiments

The photometric reduction of array data described here is more elaborate than necessary for this analysis, but the results will be used in later papers.

2.2.1. SOKP 2.3 m. The 2.3-m telescope of Steward Observatory at Kitt Peak (SOKP) observed with a 64 × 64 infrared array at a wavelength of 2.33 μm and a passband of 0.07 μm. The average frame acquisition rate was 1.91 Hz for a total of ~32,500 images during the whole event. Data acquisition was controlled by software running on an 80386 computer, and the individual 16-bit frames were written to a hard disk during observation. Two flat field frames were acquired after the event. The better of the two was normalized to 1 and divided into each SOKP frame before reduction to correct for the non-spatially uniform response of the detector.

Individual frames were time-tagged from a reference oscillator in the computer with a 2-byte coarse time stamp and a 3-byte fine time stamp. Analysis showed that the oscillator drifted with respect to UTC by approximately 250 msec during the ~8000 sec from the inbound C-ring occultations to outbound C-ring occultations and that the coarse timer, which was accurate to 1 sec, drifted relative to the fine timer. The time calibration of this experiment, like those of our other North America experiments, was ultimately obtained from cross-correlation of atmospheric scintillations, as discussed below in Section 3.

The SOKP data suffered from several other problems. Due to electrical interference, portions of the data, especially the beginning and end of the data set, were plagued by semirandomly located negative and "hot" pixels. Each image was cleaned of these pixels where possible by replacing bad pixels with a valid pixel value from the same location in a previous uncontaminated frame. All of the negative data values and all of the data values above the brightest portion of the image—the B ring—were removed in this way. Also, a horizontal striped pattern, with a wavelength of 2 lines and an amplitude of a few DN, appeared in the raw images. Finally, the histogram of these data was only half-filled: data numbers in groups 16 DN wide are present in the raw data; the following 16 data numbers are largely missing. This pattern repeats for the entire histogram and is present in all images. Since 16-bit photometric precision was clearly obviated by these problems—in fact, in signal to noice analysis, it was determined that the data contained less information than the DN values implied—all images were divided by 32 in the reduction process to eliminate the "stuck" bit.

2.2.2. UKIRT 3.8 m. Observations were made with the IRCAM at the United Kingdom Infrared Telescope (UKIRT) on Mauna Kea in Hawaii. This camera was equipped with a 62 × 58 array with a scale of 0.62 arcsec/pixel. About 24,280 16-bit frames were taken of the event at a sampling rate of 3 frames/sec. Two different filters were used during the event: the planetary occultation was observed through a CO filter with a central wave-

signal to make the output positive at all times. (In such a procedure, a constant stellar source would yield a sinusoid.) The output was sent through an A/D converter and recorded in the computer's memory every 10 msec; i.e., 10 raw voltage measurements were stored every chopper cycle for a total rate 100 samples/sec. After the accumulation of 12,800 samples, a write-to-disk operation was initiated. The data points were registered in time to an onboard oven-stabilized crystal oscillator, which was calibrated to UTC to a precision of ±1 msec in the laboratory prior to and following the occultation.

Several problems in this signal chain affected the results from these two experiments. First, the write-to-disk operation occasionally failed at both stations, causing irretrievable loss of data. Second, the bias level at both stations was not constant during the occultation but was a function of signal strength with a characteristic time of 1–2 sec. This resulted in an unreliable background level at both stations; at the MMT, it occasionally caused the signal + bias to exceed the instrument's dynamic range, clipping the output. Third, noise bursts affected from one to three consecutive samples at both stations. Furthermore, electrical noise generated by the periodic mirror alignment operations at the MMT destroyed approximately 30 sec's worth of data each time this occurred.

To rectify some of these problems, the standard method of boxcar differencing of the chopper output was discarded and a least squares fitting procedure was used. The 10 samples of each chopper cycle were fitted to one cycle of a sine curve using a model with two parameters: amplitude and bias. It was also necessary to find the absolute phase of the chopper at some selected point in the datastream to define the beginning of the cycle. This was measured once for each dataset and taken as a fixed parameter. (It was verified to be constant for the dataset by measuring it at several locations.) The amplitude was proportional to the stellar flux during that cycle; the bias was of no interest. If the residuals in these fits exceeded a certain threshold, the sample with the largest residual was rejected and the remaining points used to produce a new fit. The rejection of points continued until a good fit resulted or the number of points remaining was too small for a reliable fit ($n < 4$) in which case the flux value was marked bad. The output from the least squares procedure were then processed with a spike filter having a width of 5 flux measurements. Isolated measurements with large deviations from their neighborhood were smoothed. This procedure was able to restore many of the data points damaged through bias level and noise problems. In all, ~50% of the MMT data and ~20% of the Catalina station data were lost due to the combination of problems.

Finally, although the relative time stability of the data systems appears to be excellent, the absolute calibration failed for both the MMT and 1.54-m at the subsecond level. Absolute timing calibration was accomplished using scintillations in Saturn's atmosphere (Section 3).

2.1.2. San Pedro Mártir 2.1 m. This experiment was conducted with a filter centered at 3.23 μm with a passband of 0.104 μm and an InSb detector. A diaphragm of 7 arcsec diameter was used. Chopping was done at exactly 10 Hz, synchronized to the sampling interval. The throw was 30 arcsec North–South, with alternate chops on opposite sides of the star (three-beam chopping; Landau *et al.* 1992). Guiding was accomplished by viewing 28 Sgr through a dichroic mirror. The signal was phase-detected with a Stanford Research SR510 lock-in amplifier having an input passband filter and two output filters in cascade, each with a time constant of 100 msec. The time base was provided by a 1-kHz interrupt from a Precision Standard Time, Inc., model 1020 time source, receiving WWV UTC time signals. The propagation delay from Ft. Collins, Colorado to San Pedro Mártir was set to 4 msec and delays internal to the computer were calibrated to ±1 msec. UTC was recorded with the data every sample. Sampling times never varied by more than 1 msec. Drift scans along 28 Sgr's path through the Saturn system were made the night before the occultation. These were subtracted from the occultation scan at each spatial position to provide a first-order correction for the background flux from Saturn and its rings through the diaphragm. The background flux reached its maximum value in the B-ring, where it amounted to ~30% of the unocculted stellar flux. After the correction was applied, experimental variations in the stellar flux at the level of ~5% remained, but these variations were sufficiently gradual that they do not affect the timings analyzed here.

2.1.3. CTIO 4 m. The CTIO observations were made at the 4-m telescope through a filter centered at 3.2415 μm with a passband of 0.144 μm using a single-channel InSb dewar ("D-3") cooled to 77 K on the standard CTIO IR photometer box (Colbeck 1990). A beam-size of 8 arcsec was used; this was dictated by the relatively poor seeing at the time of the observations, roughly 2–3 arcsec in the visible. The observations were made with the telescope's chopping secondary running at a frequency of 18 Hz. The output of the dewar preamp was fed to a PAR model HR-8 lock-in amplifier. The signal from the lock-in was digitized at 10-msec intervals and pairs of data points were summed yielding an effective sampling rate of 50 Hz. These settings leave some residual modulation of the output which was removed by appropriate spectral filtering (see below), but on the other hand introduce relatively little time delay into the output. Timing signals were simultaneously recorded at 1-sec intervals; comparison with an accurate satellite clock shows that these signals were accurate to within 5 msec

ing of 80 added frames. (In the SOKP data, the summed image consisted of 40 sec's worth of data.) Only frames with fitted residuals less than 0.87 pixels were used in this process. A box centered on the ephemeris star position and sized to encompass the entire seeing disc was zeroed out before adding each frame to the summed frame. Due to the poorer seeing of the egress occultation in the SOKP data, a larger box is used for egress (14 × 14) than for ingress (8 × 8). Hot pixels whose data values were greater than the maximum data value (found in the B ring) and pixels with negative data values were excluded from the 80-frame sum. The number of data values ($\leq$80) constituting the final sum for each pixel in the summed frames was recorded in separate "count" arrays.

In order to determine the 2-dimensional ring background at any time during the occultation, all the summed frames during a certain interval centered on that time were averaged together (using the sum of the count arrays as a divisor) to form a template. The interval was chosen to be long enough that all the pixels in the vacant box created by the zeroed-out stellar position, whose location in the frame changes by ~0.005 pixels/sec, were filled in with average data values determined from the summed images taken during an interval when the star was within $\pm\sim$1.33 box-widths away. For the ingress SOKP occultation, each template was ultimately composed of images taken within ±40 min surrounding each image: i.e., between 1800 and 5000 individual measurements for each pixel in the template. Use of these "moving" templates automatically accounted for the possible changes in atmospheric transmission during the course of the occultation.

The total stellar flux was calculated by (1) expanding each image by a factor of five in each direction by simple repetition of pixels to equal the size of the templates, (2) aligning the centers of the image and the appropriate template and subtracting the template from the image, and finally (3) summing the pixel values falling within circular apertures centered on the centroid of the star's image. If the integrated stellar flux was low enough to make the calculation of the centroid unreliable (as happened at certain locations in the B ring, for example), the ephemeris star position was used. Bad pixel values (i.e., negative data values and obvious hot pixels) within the occulted stellar image were replaced with "good" pixel values taken from previous images.

2.3.2. UKIRT. The data reduction procedure for the UKIRT data was essentially the same as for SOKP except in two ways. First, the data quality (i.e., noise and dynamic range) was much better than in the Kitt Peak data set and so the extra steps of removing bad pixels and bit level requantization were not necessary. Second, the spectral filter used for the ring occultation in this data set, 3.08 μm, cut out the ring flux almost entirely, making it impossible to navigate on the rings. The fits to determine orientation and the Saturn center were consequently done using Saturn's limb. Because the rings obscure part of the southern portion of Saturn's disk, a simple calculated limb curve was insufficient. A line of constant latitude $\theta = -12.9°$, the empirically determined function which represents the projection of the rings on the disk of the planet, was combined with the functional representation of the planet's limb above this latitude to produce the calculated curve used in the fitting procedure. For the UKIRT data, the FWHM of the stellar image, and the zeroed-out box in the summed frames, were 1.5 pixels and 12 × 12 pixels, respectively. The final templates for ring background subtraction were consequently comprised of images taken within $\pm\sim$43 min of each frame, for a total of 1400 to 8000 individual measurements for each pixel in the template.

3. CALIBRATION OF TIMINGS

All three of the Tucson-area stations were afflicted by timing errors. As has already been mentioned, there was a substantial time drift at the SOKP experiment, and its absolute time calibration could only be achieved by reference to other stations. In the case of the MMT and Catalina experiments, the initial laboratory calibration to absolute time ultimately turned out to be late by approximately 0.2 sec for both sites, in the sense that the system times were too large with respect to UTC by this amount. A small discontinuity between the calibration timing offsets before and after the observing run was observed for both the MMT and Catalina, suggesting that calibration had been lost during the observations. Initially, this discrepancy was ignored.

At San Pedro Mártir (SPM), the absolute time calibration worked well and gave consistent results for the event times. However, there was a substantial instrumental time delay due to the two output filters in cascade which had the effect of imposing an offset on the order of 0.2 sec on the real event times. Because this time offset was very nearly equal in sign and magnitude to the erroneous time calibration at the MMT and Catalina, it was possible to obtain a very consistent (and totally erroneous) fit to the ring events using the timings from the three Tucson stations, SPM, and CTIO, with the SPM time delay ignored. A result indicating substantial deviation from both the Simpson (1983) and NCP poles was derived from this initial analysis (Hubbard *et al.* 1990b). However, comparison with the NE set of ring timings yielded strong evidence for substantial errors in the Tucson-area timings, including the fact that the SPM time delay was a non-negligible effect.

length of 2.33 μm and a passband of 0.08 μm; a filter centered on a water ice absorption at 3.08 μm with a 0.03-μm passband was used during the ring occultation.

Owing to the timing and the geometry of the event in Hawaii and restrictions on the minimum elevation of the UKIRT, ingress through the rings was not observed. Dark and bias frames were taken before the event to determine the level of dark current and the bias voltage applied to the array, respectively. Data acquisition of the planetary occultation began with the CO filter at 7:16 UTC and ran until 8:37:11 UTC when the filter was changed (A bias frame was taken toward the end of this interval). Data acquisition resumed at 8:37:41 with the ice filter and continued until about 9:41 UTC. After the occultation, additional bias and dark frames were taken. In addition, flat frames were taken through the CO filter using the telescope dome and the sky as flat fields; only dome-flats were taken through the ice filter.

The dark current frames taken during the course of the occultation were used to form an average dark frame. The bias frames were averaged together and the resulting averaged bias was subtracted from the averaged dark frame, and from the raw data images. The averaged bias frame was also subtracted from the flat frames, which were then summed and normalized to one. (For the CO frames, only the CO sky flats were used.) All these bias-subtracted frames—dark, flat and raw data—were corrected for the fact that the chip had a nonlinear response to signal. The final, reduced form of each image was achieved by subtracting the averaged dark and dividing by the appropriate normalized flat.

2.3. *Conversion of Imaging Data to Occultation Scans*

Because of the two-dimensional nature of the array data, they held the greatest promise for precise subtraction of the ring light contribution to the integrated stellar flux. We developed a batch-oriented array data reduction procedure which took advantage of this characteristic by forming and subtracting a map of the rings or "template" from each image in the data set, integrating the remaining stellar signal and ultimately converting the sequence of images into a scan of transmitted stellar flux versus time. At the heart of this procedure is a "navigation" algorithm, originally developed to correct camera pointing on Voyager spacecraft images, which determines the line and sample (l,s, respectively) coordinates of Saturn's center and the orientation of the planet's spin pole in the image by utilizing the observing geometry and the absolute size and shape of some planet-centered feature such as the limb or a ring. This iterative least-squares procedure calculates the line and sample displacements required to align a mathematical 2-dimensional representation of the feature with the actual feature in the image. The fit is considered good if (a) the residuals are less than 0.7 pixels and the star's measured position is within 3 pixels of the position predicted using the stellar offset ephemeris and the Saturn center coordinates determined by the fit or (b) if the residuals were less than 0.5 pixels in those cases when the star's centroid could not be confidently measured. The starting point for the entire sequence of images was determined by fitting the first image interactively. The program uses the last good fit from a previous image as a starting point for the next image.

2.3.1. SOKP. In navigating on any reference, it is best to use as much of the full curvature of the feature as possible. Saturn's disk is dark at 2.33 μm, leaving the rings as the only constant reference in the SOKP images. Several images taken from the middle of the occultation show nearly the entire ring system. The resolution in these groundbased images is very low, ~4000 km/pixel, so only major ring features and boundaries are easily distinguished. Consequently, the outer edge of the A-ring and the inner edge of the B-ring were used as references to determine the best-fitting image scale of 0.56 arcsec/pixel; the edge of the A-ring was fitted by the algorithm described above to determine the ring pole orientation for the entire data set.

Since the array experiments were guided on 28 Sgr, the disk of Saturn moved across the array during the occultation at a rate of ~20 km/sec or ~0.005 pixels/sec. Consequently, the center of Saturn had to be determined for *every* image, including those in which less than half of the ring system is seen. To achieve automatic determination of the Saturn center coordinates and to mitigate the problem of a limited ring curve in most frames, we fitted to two features in the SOKP images: the outer edge of the A ring and the entire B ring. The latter has approximately a Gaussian shape in these low-resolution frames. Thus, the two functions stored for fitting were a ring edge, represented by a step function convolved with a Gaussian function of $\sigma \sim 0.85$ pixels determined from the star's seeing disc, and a Gaussian curve centered on the B ring with a full width half maximum determined from the images. The image scale and pole orientation determined initially were kept constant. The algorithm saves the planet center's (l,s) coordinates, usually determined to a precision of ~0.4 pixels, the star's (l,s) determined from a fourth-order polynomial fit to the ephemeris of the star/planet-center offset, and the number of points used in the fit.

The next step in the array data reduction was the subtraction of the ring background from each image. The images were expanded to five times their original scale by simple repetition of pixels to take advantage of the subpixel fitting accuracy, registered on the planet's center, and then added together to form a summed image consist-

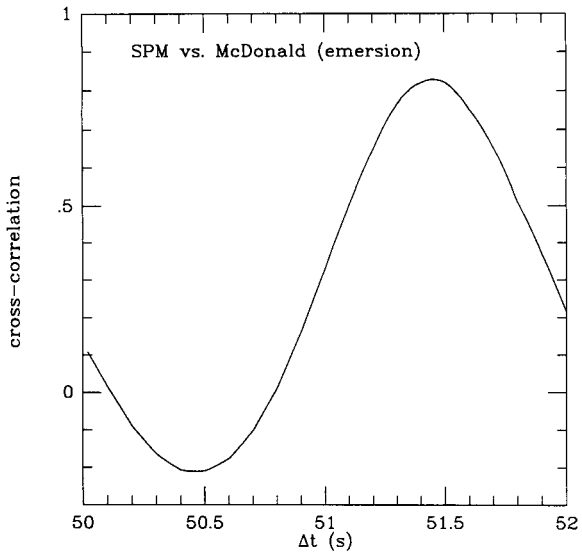

FIG. 5. Cross-correlation of Saturn atmospheric scintillations observed at SPM (station 4) and McDonald.

cross-correlation of 0.83 at a time offset of $+51.46 \pm 0.02$ sec to the system time of McDonald with respect to SPM. The presence of this large correlation, despite the 50-sec propagation time of the limb shadow from west Texas to Baja California, is in itself of considerable scientific interest and will be further discussed elsewhere.

Every possible permutation of cross-correlations between stations was calculated (immersion was not observed at the MMT). In general, maximum values of about 0.8 were found for the cross-correlation of each pair of stations, and these peak values defined a time offset to a precision of ~0.02 sec. The cross-correlations between the most distant stations (McDonald vs SPM, Tucson-area vs McDonald) were for some reason somewhat poorer for the immersion lightcurves, reaching a peak value of about 0.5, and in one case (McDonald vs SPM, immersion) there were two nearly equal peaks at about 0.5. The changes in cross-correlations of scintillations may be related to the physics of the underlying disturbances in Saturn's atmosphere, but this topic lies beyond the scope of the present paper. As discussed below, all of the time offsets gave consistent results, and in the case of dual peaks it was obvious which one was meaningful.

We then arbitrarily chose a half-light time for a single reference station and, using a provisional center for Saturn, computed the trajectory of a projected oblate atmospheric level surface which passed through this point on the station track. The observed values of Δt at maximum correlation were then applied to the system times of the other stations, and a further correction to the system time was applied in order to shift the point on the station track to lie on the common level-surface trajectory. Since we may apply only one correction to the system time for each station after the first, but we have constraints at both immersion and emersion, the problem is overconstrained. The optimal solution was found by minimizing the squares of the distances from the level surface with respect to the system time corrections. The optimized solution was extremely consistent, with maximum deviations from the common level surface smaller than 0.5 km. From these results we infer an absolute correction to the MMT system time of -0.14 sec, to the Catalina system time of $+0.37$ sec, and to the SPM system time of -0.29 sec. Our confidence in these calibrations is ± 0.02 sec. In the case of SOKP, we obtained separate corrections for the system time at atmospheric immersion and emersion. These were -16.33 and -16.58 sec, respectively. These corrections were respectively applied to fiducial ring events prior to atmospheric immersion and after atmospheric emersion—since there was evidence that the SOKP system clock changed discontinuously some time during mid-occultation by Saturn—and were assumed constant during the respective interval.

The corrections tie the four stations MMT, Catalina, SOKP, and SPM to the McDonald time base; we assume that the latter has zero error with respect to UTC. There is independent evidence that this calibration is valid: (1) the inferred correction to the SPM system time is entirely consistent with an instrument delay imposed by two 100-msec filters in cascade; (2) the stellar radius inferred from the ring edge events (see below) at SPM is significantly larger than the values inferred from the other stations, but becomes consistent with the value from other stations when a correction based on the inferred time delay is applied; (3) the calibrations result in a smooth fit of all stations to the optimal ring solution, with little or no systematic trend in residuals evident at any station.

Finally, an instrumental correction was applied to the CTIO data, based on the 110-msec time constant described in Section 2.1.3. When the feature-timing method discussed in the next section was applied to a stellar profile convolved with a 110-msec exponential time delay, the half-flux time was delayed by 100 msec, whereas the inferred stellar radius was increased by 4%. Thus the CTIO system times for fiducial features have been corrected to UTC by -0.10 sec, and the inferred stellar radius reduced by the appropriate factor.

4. TIMING OF FEATURES

A reasonably model-independent time for occultation by a sharp ring edge can be specified by $t_{1/2}$, the time at which the observed flux from 28 Sgr reaches the mean of the value just before the ring edge contacts the stellar disk and the value just after the ring edge completely covers the stellar disk. We have found that at the wave-

We have ultimately relied upon the occultation data set to calibrate the Tucson and SPM timings, as is also done in the NE paper. However, our calibration method is entirely different from NE. In the NE paper, corrections to times are derived by improving the fits to the ring data. Our preference is to minimize correlation by deriving these corrections independently of the ring data, since the corrections have a major effect on the ultimate ring pole. Our calibration uses Saturn's atmosphere as a calibration reference, making almost no use of ring timings. As Figs. 1 and 2 show, the occultation chords were nearly normal to Saturn's atmosphere because of the near-central geometry. This is unlike the situation for the ring occultations, where the occultation chords deviate substantially from normal incidence to the rings, particularly during the inbound occultations (Fig. 1). Thus the relative times of first and last contact with Saturn's atmosphere, at closely adjacent stations, are reasonably insensitive to the precise placement of the center of Saturn. In this case, a provisional position for the center, not very sensitive to the ring geometry, can be used to predict the relative contact times. Figure 4, a further enlargement of a section of Fig. 2, shows the chords at Saturn's immersion limb for the North American stations, including the Palomar and McDonald stations of NE. Tick marks (every 10 sec) show the computed positions of the stations as a function of UTC. Atmospheric immersion and emersion were not observed at Palomar, so we do not discuss this station further.

Inasmuch as the maximum separation among all the North American stations projected along the planet's limb—i.e., the distance between Catalina and McDonald—does not exceed 200 km, one would expect

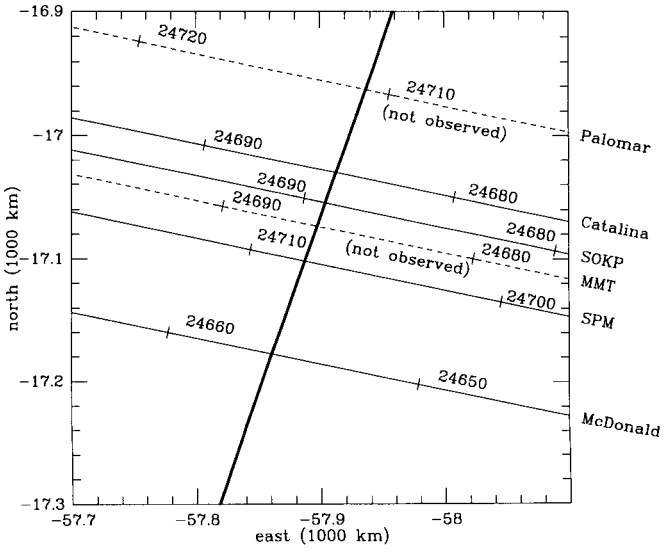

FIG. 4. Expanded view of the immersion limb for North American stations in Fig. 2. Heavy line is Saturn's limb.

good correlation between the atmospheric occultation lightcurves among all these stations. As is now well known (French *et al.* 1982, Narayan and Hubbard 1988), stellar occultations by planetary atmospheres typically show strong scintillations, which are produced by small density inhomogeneities projected along the line of sight. These inhomogeneities and the attendant scintillations are highly anisotropic, with aspect ratios (horizontal to vertical) on the order of 10^2: i.e., the turbulent elements are aligned with their long axis parallel to the atmospheric limb and normal to the projected gravity vector. Detailed studies of anisotropic inhomogeneities in the upper atmosphere of Uranus (French *et al.* 1982) and Neptune (Narayan and Hubbard 1988) confirm large aspect ratios in both planets; we assume here that similar values apply to Saturn.

For a projected stellar radius on the order of 10 km, much of the scintillation power arises from elements with short axis dimensions of roughly the same size. These same elements may then be expected to persist for ~1000 km parallel to the limb. It follows that a given scintillation that is observed at several stations separated by ~100 km along the limb should coincide closely with a level surface in the planetary atmosphere. Quantitatively, if the inclination of the scintillation to a projected level surface is $\sim 10^{-2}$ radians, roughly equal to the anisotropy factor, then the maximum misalignment of two stations separated by ~100 km would be ~1 km. Since we align stations by utilizing measurements of 10 or more random scintillations during atmospheric immersion or emersion, the alignment uncertainty is reduced below 1 km. We assign a probable error of ±0.4 km to the scintillation alignments, corresponding to a probable error in the time calibrations of ±0.02 sec.

We find that there is in general good cross-correlation between the scintillations observed at our four North American stations and at the McDonald station of NE. The cross-correlation is calculated as follows. We first perform a least-squares fit of a standard Baum–Code occultation lightcurve to a normalized immersion or emersion event, adjusting the two parameters of half-light time and atmospheric scale height. The residuals with respect to the best-fit lightcurve are then tabulated over a time interval of approximately 50 sec near half light, when the scintillations are strongest, and at the maximum time resolution of the data set, typically 0.1 sec. The mean of the residuals over this interval is then subtracted from each individual residual to give a new residual table with zero mean. The zero-mean residuals are then normalized to unit variance, and the cross-correlation function of the residuals between two stations $C(\Delta t)$ is then calculated as a function of the time offset Δt. Figure 5, the cross-correlation function for SPM emersion with respect to McDonald emersion, is a typical result showing a maximum

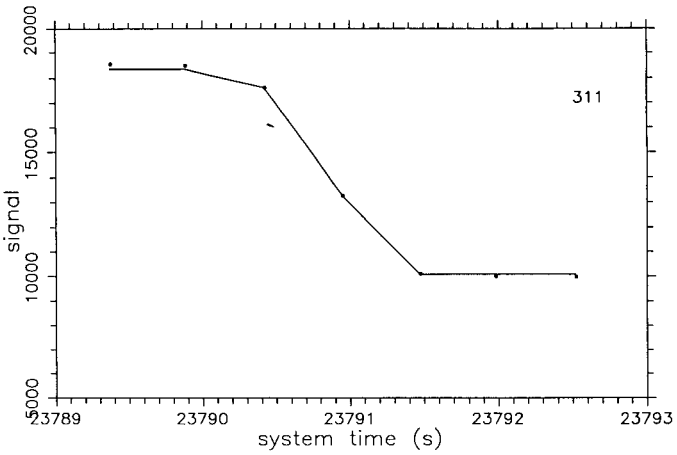

FIG. 8. Data (points) and model (solid line) for the inbound occultation of 28 Sgr by fiducial feature 1, observed at SOKP (station 3).

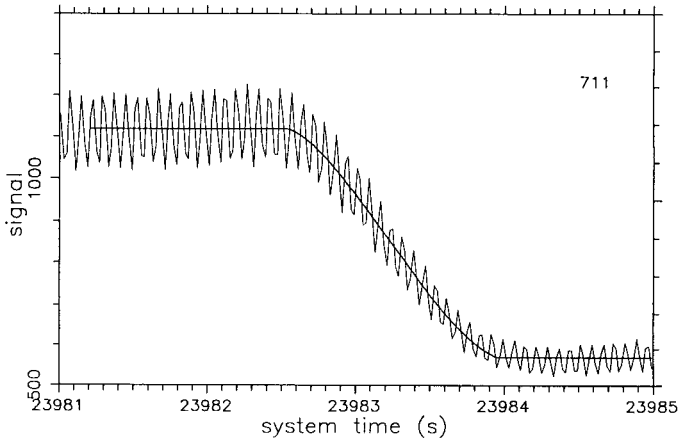

FIG. 10. Data (light line) and model (heavy line) for the inbound occultation of 28 Sgr by fiducial feature 1, observed at CTIO (station 7). The unfiltered signal is displayed.

linear interpolation. When calibrated against the radius-modeling program, the latter program gave consistent values of $t_{1/2}$ to within ± 0.01 sec.

Table III lists the final timings derived from each of our experiments for the set of 18 fiducial ring features. Sixteen of these—12 in the outer C ring, 3 in the Cassini Division, and the outer edge of the Keeler gap—were found to be circular to the ± 2-km level in previous searches for eccentric Saturnian rings (Porco and Nicholson 1987, NCP, Cooke *et al.* 1992). The remaining two features—the edges of the Encke gap—are known to exhibit edge waves with peak-to-peak radial amplitudes of 4 km and an azimuthal wavelength of 1800 km (0.7°) but limited azimuthal extent (Cuzzi and Scargle 1985). In the final astrometric solution, these two features (along with the Keeler gap outer edge) provided strong leverage for solution radii in the A ring and exhibited residuals that were no larger than other presumably circular features.

In Table III, the column marked 'im./em.' denotes whether the event was observed prior to atmospheric immersion (1) or after emersion (2). Values of $t_{1/2}$ have been corrected to UTC as described above. Each event is denoted by the indices i, j, k, where i corresponds to the station number (first column in Table III), j corresponds to the ring number (second column), and k (third column) indicates whether the event was preimmersion or post emersion. The column R_{28} denotes the radius of the fiducial feature from the center of Saturn obtained from the 28 Sgr timing, using the model which we describe below and the NCP pole, whereas $\delta R = R_{28} - R_{\mathrm{NCP}}$. All of the timings entered in this table are those used in our analysis; we have not included any of the rejected timings.

All stations gave consistent results for the projected stellar radius r_*, with only a weak dependence on the precise choice of astrometric solution. Figure 11 shows the average value and standard deviation of r_* at each

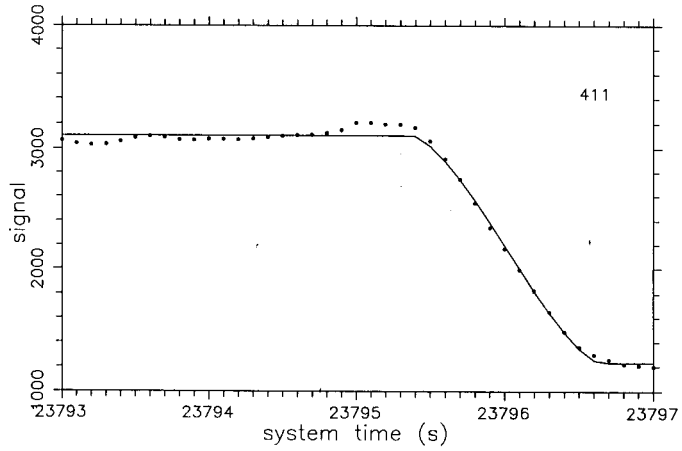

FIG. 9. Data (points) and model (solid line) for the inbound occultation of 28 Sgr by fiducial feature 1, observed at SPM (station 4).

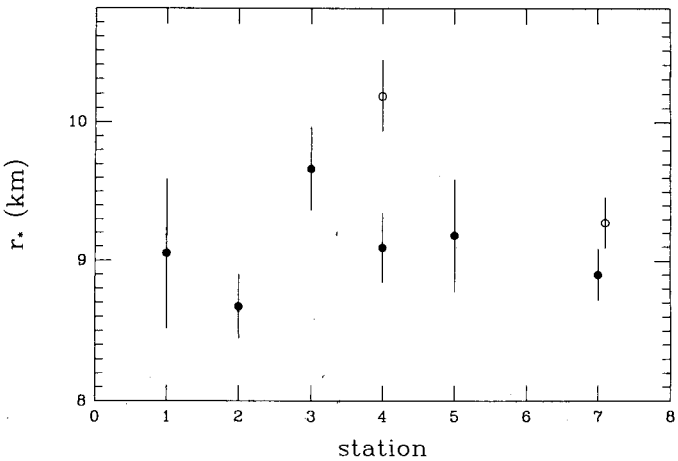

FIG. 11. Radius of 28 Sgr as measured at our stations.

lengths of observation used here 28 Sgr can be well represented as a uniformly illuminated disk of apparent radius r_* projected above the limb of Saturn. Our model for the variation of the total signal S as a function of time t is

$$S = S_2 + (S_1 - S_2)F(t), \tag{1}$$

where S_1 is the signal before occultation, and S_2 is the signal after full occultation ($S_1 > S_2$). Consider a disk of radius r_* that is partially covered by a knife edge at distance xr_* from the disk's center, and let F represent the fraction of the disk's area that is uncovered by the knife edge, defined such that $F = 1$ for $x < -1$ and $F = 0$ for $x > 1$. A simple calculation then gives

$$F = \frac{1}{\pi}(\cos^{-1} x - x\sqrt{1 - x^2}); \tag{2}$$

and $|x| \leq 1$, and we can write

$$x = \frac{v_\perp(t - t_{1/2})}{r_*}, \tag{3}$$

where $v_\perp$ is the velocity component of the star image normal to the ring edge, projected in the sky plane (which is defined as the plane normal to the vector from observer to star and containing the body center of Saturn).

Equations (1)–(3) specify a model flux in terms of the four parameters, S_1, S_2, r_*, and $t_{1/2}$. The parameters S_1 and S_2 vary from one ring edge to the next because of variable background ring opacity and scattering into the aperture. However, they can usually be considered constant during the brief interval of duration ~1 sec for which $|x| \leq 1$, the critical interval for determining r_* and $t_{1/2}$. The parameter $t_{1/2}$ is essentially uncorrelated with r_*; the latter should have the same value for all occultations by sharp edges. A fifth parameter, $v_\perp$, is known in advance quite accurately once the full astrometric solution has been self-consistently determined.

Although the parameter r_* has no direct bearing on the timings of edge features, it serves as a useful monitor of the validity of a given timing, since a fully self-consistent set of measurements should give the same value of r_* for each edge event. Timings which gave a value of r_* more than a few standard deviations away from the best-fit result were rejected. Most such rejected observations were obviously affected by poor guiding or instrumental problems. In a small number of cases, values of r_* were too large to be plausible, yet there was no clear evidence of any other problem. Although it is possible that the ring edge was locally fuzzy for these events, we chose to ignore them for this analysis.

The stellar profile model fits the data quite well. Figures 6–10 show the same ring edge (ring 1 inbound) observed at five stations, together with the model profile. Although some limb darkening may be present, it is not needed to fit the data. Diffraction is also unimportant in this data set, as the Fresnel scale $\lambda_F = \sqrt{\lambda D} = 2$ km $\ll r_*$ (D, distance to Saturn). There is no evidence for any asymmetry in the projected disk of 28 Sgr nor for any close companion star. 28 Sgr is known to have a distant companion 7.7 magnitudes fainter at a separation of 13.7 arcsecs; this companion would not have been included in the aperture of aperture experiments and is too faint to have significantly affected the array results for purposes of the present paper.

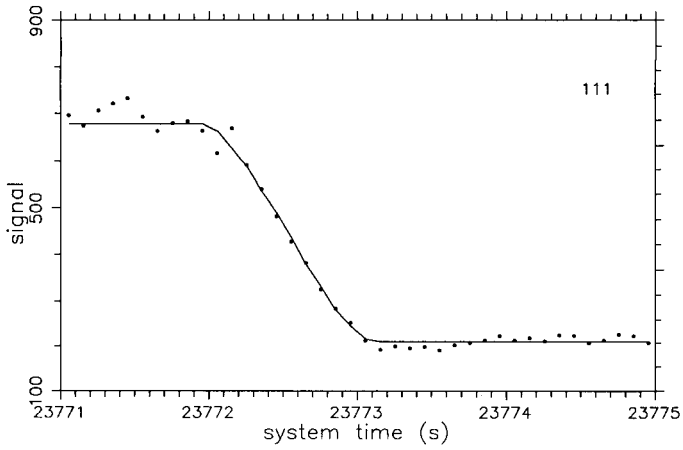

FIG. 6. Data (points) and model (solid line) for the inbound occultation of 28 Sgr by fiducial feature 1, observed at MMT (station 1).

In the case of some features in the Cassini Division (features 19, 20, 21 in Table III) which could not be adequately represented by Eq. (2), it proved to be more accurate and efficient to measure the half-flux times without modeling the stellar radius. This was done with a program that establishes the values S_1, S_2 and finds $t_{1/2}$ by

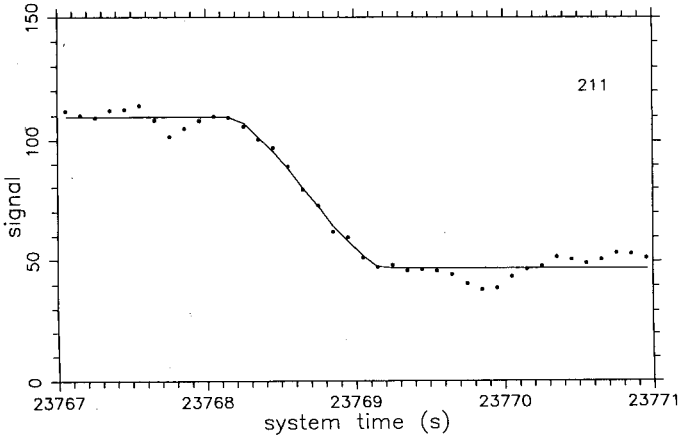

FIG. 7. Data (points) and model (solid line) for the inbound occultation of 28 Sgr by fiducial feature 1, observed at Catalina (station 2).

station. Open symbols for stations 4 (SPM) and 7 (CTIO) show values before correction for the instrumental time constant, whereas solid symbols represent final values. The weighted mean of all stations is $r_* = 9.01 \pm 0.25$ km. This result is consistent with the apparent magnitude, spectral type, and luminosity class of 28 Sgr, assuming that the star is at a distance ~100 parsecs.

5. ASTROMETRIC SOLUTION

(a) *Procedures and Coordinate Systems*

The data analysis requires that each timing of a ring edge, $t_{1/2}$, be mapped onto a radius R_{28}, where R_{28} is the radius from the center of Saturn at which the photon received at $t_{1/2}$ pierced Saturn's equatorial plane during the 28 Sgr occultation. This calculation is carried out using two coordinate systems: a fixed celestial coordinate system (α_{2000},δ_{2000}) using the equator and equinox of 2000.0, and an apparent coordinate system (α,δ) of date.

First, for a given UTC time t, we computed the apparent coordinates of 28 Sgr (α_*, δ_*) and apparent geocentric coordinates of the Saturn barycenter (α_S,δ_S), together with D, the true distance from the geocenter to the Saturn barycenter. The apparent star coordinates were computed from an assumed position $\alpha_{*,2000} = 18^h46^m20.605^s$, $\delta_{*,2000} = -22°23'31.83''$ (Mink, personal communication, 1989), whereas the Saturn coordinates were kindly furnished by S. Newhall (personal communication, 1989). The latter are fully equivalent to, but are given to more significant figures than, the Saturn barycenter ephemeris published in the *Astronomical Almanac* (1989). To compute the apparent geocentric stellar positions, which incorporate the effects of stellar aberration and terrestrial precession and nutation, we used results from the 1989 *Astronomical Almanac*, as incorporated in software form and distributed as the interactive computer ephemeris (ICE). However, the ICE and the *Astronomical Almanac* only give apparent stellar positions to the nearest 0.001 sec in right ascension and 0.01″ in declination, which is adequate for many occultations, but not this one. The roundoff error associated with this precision amounts to several kilometers over the duration of the event. To smooth the results and thus reduce roundoff error to an acceptable level, we tabulated apparent stellar positions at hourly intervals for several days centered on 3 July 1989 and least-squares fitted the positions with a smooth polynomial in time.

We then computed the predicted differences in right ascension $\Delta\alpha$ and declination $\Delta\delta$ of the star with respect to the Saturn barycenter, as observed from the geocenter. These were converted to station-centered differences by using the known latitude, longitude, and elevation of each station, and the declination and hour angle of 28 Sgr at the station. Next we converted the differences in apparent coordinates to differences in the fixed J2000.0 coordinate system by applying corrections for differential precession, aberration, and nutation using a polynomial fit to the values given in the 1989 *Astronomical Almanac*. We denote the resulting differences in right ascension and declination, respectively, as $\Delta\alpha_{2000}$ and $\Delta\delta_{2000}$.

The J2000.0 east and north linear offsets projected in the sky plane of the star with respect to the Saturn *body* center, x_0 and y_0, respectively, are computed using

$$x_0 = D' \, \Delta\alpha_{2000} \cos \delta_{S,2000} + \Delta x_0, \tag{4}$$

$$y_0 = D' \left(\Delta\delta_{2000} + \frac{1}{2} \cos \delta_{S,2000} \sin \delta_{*,2000} \, \Delta\alpha^2_{2000} \right) + \Delta y_0, \tag{5}$$

where D' is the distance from the observer to Saturn, backdated for the light propagation time, and $\delta_{S,2000}$ denotes the declination of the Saturn barycenter in J2000.0 coordinates. We incorporate an additional small correction Δx_0, Δy_0 for the Saturn body center offset from the barycenter, computed for us by W. Owen of JPL using the ephemerides for Saturn and each of its satellites (JPL Ephemeris File SAT018H.NIO). The size of this correction is of order 300 km and varies by ~30 km over the period of the occultation. Expressions (4) and (5) represent an expansion in $\Delta\alpha_{2000}$, $\Delta\delta_{2000}$ to second order in the differences. Normally only a first-order expansion is required for planetary occultations, but not in this case. Because of the large values of the differences, neglect of the second-order terms leads to errors at the level of several kilometers.

Once x_0,y_0 are known, we compute the general relativistic bending angle ε_G in the x,y plane, giving a corrected position for the pierce point of the photon in the sky plane,

$$x = x_0 - D'(\varepsilon_G)_x, \tag{6}$$

$$y = y_0 - D'(\varepsilon_G)_y, \tag{7}$$

where expressions for ε_G are given below.

Next, we compute the position angle p of the normal to the ring plane, projected in the plane of the sky, and the angle B which the vector directed to 28 Sgr makes to Saturn's equatorial plane. These angles are computed from the J2000.0 positions of 28 Sgr and the assumed J2000.0 coordinates of Saturn's pole, (α_p, δ_p):

$$\sin B = -\sin \delta_p \sin \delta_{*,2000} - \cos \delta_p \cos \delta_{*,2000} \cos(\alpha_p - \alpha_{*,2000}), \tag{8}$$

and

$$\sin p = \cos \delta_p \sin(\alpha_p - \alpha_{*,2000})/\cos B. \tag{9}$$

TABLE III
Timings and Fits to Fiducial Ring Features

Sta.	ring	im./em.	$t_{1/2}$ (UT s)	δR (km)	R_{28} (km)	r_* (km)
1	1	1	23772.39	2.18	90617.34	9.16
1	2	2	31801.14	−3.01	90401.55	11.65
1	3	1	23802.81	−0.20	89939.71	6.72
1	4	2	31773.38	−2.04	89785.89	9.84
1	6	2	31746.45	−0.61	89188.68	8.69
1	11	1	24027.01	−2.45	84948.00	7.99
1	12	2	31546.20	−0.63	84749.23	9.31
1	19	1	22364.04	2.75	122050.32	–
1	19	2	33226.34	−1.86	122045.72	–
1	20	1	22502.14	−0.96	118964.08	–
1	20	2	33087.57	−2.28	118962.76	–
1	21	1	22517.04	3.97	118631.13	–
1	21	2	33072.34	−2.75	118624.41	–
2	1	1	23769.07	−2.10	90613.06	7.76
2	1	2	31809.35	−3.54	90611.63	8.69
2	2	1	23778.49	−1.34	90403.22	8.18
2	3	1	23799.33	−0.89	89939.02	9.02
2	3	2	31779.08	0.39	89940.30	9.56
2	4	1	23806.14	−0.59	89787.34	6.99
2	4	2	31772.17	−0.87	89787.06	7.93
2	6	1	23833.02	−0.61	89188.67	9.34
2	7	1	23859.67	0.07	88595.18	8.25
2	8	1	23949.20	−1.25	86601.82	9.07
2	10	1	23987.06	−0.57	85759.09	10.60
2	11	1	24023.46	−1.46	84948.99	8.22
2	12	1	24032.47	−1.37	84748.49	8.08
2	12	2	31544.91	−1.14	84748.71	8.30
2	14	1	21713.05	2.58	136524.24	10.28
2	17	2	33737.11	−4.81	133419.42	8.49
3	1	1	23774.52	1.91	90617.08	8.61
3	1	2	31813.11	−0.76	90614.40	8.87
3	2	1	23784.12	−1.34	90403.21	11.51
3	3	1	23804.88	0.85	89940.76	8.12
3	3	2	31782.68	−0.52	89939.39	8.75
3	4	1	23811.81	−1.54	89786.39	11.01
3	4	2	31775.77	−1.81	89786.12	10.74
3	5	1	23833.81	0.10	89296.37	7.59
3	5	2	31753.56	−2.78	89293.49	7.82
3	6	1	23838.65	−0.71	89188.57	9.22
3	6	2	31748.74	−2.70	89186.58	13.71
3	7	1	23865.26	0.81	88595.93	7.73
3	8	1	23954.80	−0.87	86602.20	10.55
3	8	2	31632.15	−2.01	86601.06	10.59
3	9	1	23965.24	−0.98	86369.78	10.16
3	9	2	31621.69	−1.62	86369.14	10.20
3	10	1	23992.65	−0.03	85759.63	7.75
3	11	1	24029.02	−0.31	84950.14	9.96
3	11	2	31557.58	−2.61	84947.84	10.19
3	12	1	24038.08	−1.35	84748.51	8.60
3	12	2	31548.64	−0.19	84749.67	10.71
3	16	1	21842.90	3.86	133749.35	9.90
3	17	1	21857.22	4.88	133429.11	10.02
4	1	1	23795.72	−0.55	90614.61	9.25
4	2	1	23805.23	−1.86	90402.70	11.44
4	2	2	31819.48	4.19	90408.75	11.35
4	3	1	23826.02	−0.45	89939.47	8.73
4	3	2	31798.45	1.94	89941.85	10.73
4	4	1	23832.96	−3.09	89784.84	11.41
4	4	2	31791.56	0.96	89788.89	9.92
4	5	1	23855.01	−2.69	89293.58	9.13
4	5	2	31769.48	2.44	89298.71	12.92
4	6	1	23859.75	−1.30	89187.98	11.21
4	6	2	31764.61	1.32	89190.60	9.05
4	7	1	23886.41	−1.03	88594.08	8.43
4	7	2	31737.73	−1.20	88593.92	10.01
4	8	1	23975.90	−2.11	86600.97	10.18
4	8	2	31648.01	−0.45	86602.62	14.00
4	9	1	23986.31	−1.60	86369.16	9.58
4	9	2	31637.66	2.18	86372.94	7.48
4	10	1	24013.79	−2.36	85757.30	9.70
4	10	2	31610.03	0.17	85759.83	9.14
4	11	1	24050.09	−1.30	84949.16	8.93
4	11	2	31573.60	1.08	84951.53	11.71
4	12	1	24059.10	−1.27	84748.59	10.70
4	12	2	31564.45	−1.33	84748.53	9.14
4	14	1	21740.30	1.73	136523.40	9.90
4	14	2	33893.52	−0.75	136520.92	11.04
4	16	1	21864.48	0.32	133745.82	9.78
4	16	2	33768.75	−0.12	133745.38	10.89
4	17	1	21878.92	−1.37	133422.85	9.33
4	17	2	33754.27	−0.96	133423.27	10.28
4	19	1	22387.51	3.34	122050.91	–
4	20	1	22525.51	1.46	118966.50	–
4	20	2	33104.31	0.68	118965.72	–
4	21	1	22540.61	1.87	118629.04	–
4	21	2	33089.11	0.49	118627.66	–
5	1	2	33089.11	0.16	90615.33	8.92
5	2	2	33089.11	−0.51	90404.05	11.28
5	3	2	33089.11	−0.46	89939.45	7.78
5	4	2	33089.11	−1.40	89786.53	9.45
5	5	2	33089.11	−1.65	89294.62	9.14
5	6	2	33089.11	−0.60	89188.68	10.08
5	7	2	33089.11	0.91	88596.03	8.14
5	8	2	33089.11	−1.59	86601.48	9.91
5	9	2	33089.11	0.29	86371.06	10.58
5	10	2	33089.11	−2.20	85757.46	9.57
5	11	2	33089.11	4.97	84955.42	9.39
5	12	2	33089.11	4.80	84754.66	9.98
5	14	2	33089.11	−0.33	136521.34	9.05
5	16	2	33089.11	−2.45	133743.05	8.74
5	17	2	33089.11	−2.98	133421.25	7.90
5	19	2	33089.11	0.33	122047.90	13.00
5	20	2	33089.11	−0.40	118964.64	8.17
5	21	2	33089.11	1.27	118628.44	4.20
7	1	1	23983.15	1.23	90616.39	8.93
7	1	2	31825.62	2.02	90617.19	9.78
7	2	1	23993.05	−0.18	90404.38	10.48
7	2	2	31815.65	1.18	90405.74	11.25
7	3	1	24014.73	0.35	89940.26	8.43
7	3	2	31793.74	1.29	89941.20	8.44
7	4	1	24021.88	−0.69	89787.24	9.47
7	4	2	31786.53	0.44	89788.37	9.94
7	5	1	24044.83	−0.02	89296.25	9.23
7	5	2	31763.34	0.70	89296.97	10.96
7	6	1	24049.82	0.24	89189.53	8.73
7	6	2	31758.32	1.34	89190.62	9.47
7	7	1	24077.58	0.91	88596.03	8.75
7	7	2	31730.27	1.47	88596.58	9.07
7	8	1	24170.95	−0.50	86602.57	8.94
7	8	2	31636.05	0.56	86603.63	9.30
7	9	1	24181.77	1.09	86371.85	9.03
7	9	2	31625.12	1.93	86372.69	9.62
7	10	1	24210.44	1.14	85760.80	8.74
7	10	2	31596.19	2.02	85761.68	10.03
7	11	1	24248.48	0.26	84950.71	9.25
7	11	2	31557.80	1.02	84951.47	9.88
7	12	1	24257.89	0.58	84750.44	8.84
7	12	2	31548.32	1.65	84751.51	9.34
7	14	1	21871.67	2.40	136524.07	9.47
7	14	2	33963.53	0.95	136522.62	9.74
7	16	1	21998.18	1.07	133746.57	8.98
7	16	2	33835.18	1.15	133746.65	8.72
7	17	1	22012.78	1.96	133426.19	9.05
7	17	2	33820.28	0.26	133424.49	8.95
7	19	1	22532.18	3.98	122051.56	12.18
7	19	2	33293.41	0.94	122048.52	–
7	20	1	22673.39	2.74	118967.78	6.62
7	20	2	33150.41	1.99	118967.02	–
7	21	1	22688.94	1.28	118628.44	6.49
7	21	2	33134.59	−0.86	118626.31	–

red solution which we discuss below. We assumed that the correction from UTC to dynamic time (the argument of the ephemeris given in the *Astronomical Almanac*) was ΔTT = TDT − UTC = 56.5 sec. This value is not critical as a small uncertainty is absorbed in $(\Delta x_E, \Delta y_E)$.

In our best-fit solution to the pole, we include all events listed in Table III, augmented by the timings from Palomar, McDonald, and IRTF for the same values of j, k, respectively given in Tables III, IV, and V in NE. We refer to this augmented set of timings, with unit weight assigned to each event, as the standard data set. The radii for all fiducial features were kept constant at the values given by NCP: $R_F = R_{NCP}$, as given in Table I. Although some solutions were attempted with the fiducial radii allowed to vary, we found that strong correlations between the pole position and the fiducial radii prevented finding a stable solution using the 28 Sgr data only. Thus we have used spacecraft-derived results for the fiducial radii to break this correlation.

The best-fit result for the pole position, in J2000.0 coordinates, is

$$\alpha_p = 40.59909°, \qquad \delta_p = 83.53629°, \tag{16}$$

with $(\delta R)_{rms} = 1.670$ km. Using the scatter from this best-fit solution to define the expected variance for each event, we computed the value of χ^2 for a grid of pole positions, and found the locus of χ^2 corresponding to 80% probability that the value of χ^2 was lower than the value on the locus. This locus is the elliptical contour shown in Fig. 12, which exhibits various solutions for Saturn's pole. The solution given by expression (16) is shown as a solid triangle. The contour shown in Fig. 12 also essentially corresponds to the domain occupied by pole solutions when the standard data set times are randomly varied with a gaussian distribution of timing errors, with a standard deviation of 0.1 sec (spatially, about 2 km). As is evident from Fig. 12, both the NCP pole and the earlier Simpson pole are consistent with the timings to within the uncertainties, assuming that the NCP radius scale is correct.

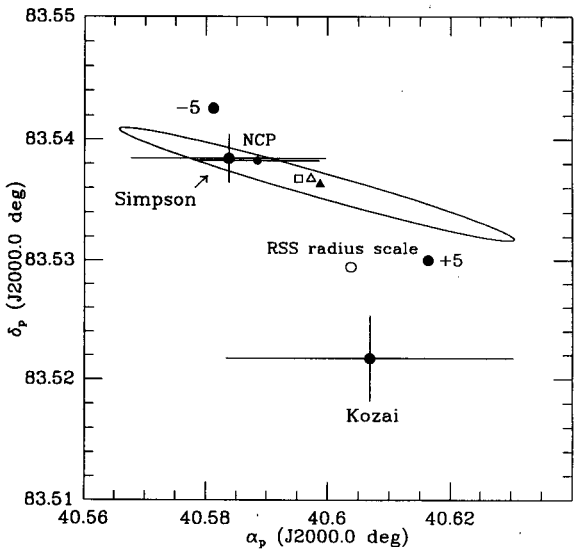

FIG. 12. Solutions for Saturn's pole, compared with previous analyses (data points with error bars). See text for details.

Next, we calibrated our solution against the NE solution by changing only the star position. We adopted the J2000.0 position and apparent positions of 28 Sgr calculated by NE so as to exhibit most cleanly the differences in the basic astrometric algorithms. Again using the standard data set and our algorithm, but the slightly different star position, we obtain a pole position indicated by the open triangle plotted in Fig. 12. For comparison, the equivalent pole position calculated by NE using their algorithm is plotted as an open square. The difference in pole positions is less than 1 arcsec and is well within the basic uncertainty of the measurements.

The 28 Sgr data set alone do not constrain the pole position and ring radius scale independently because these quantities are highly correlated. To illustrate the sensitivity to the radius scale, we show in Fig. 12 the best-fit pole positions which are derived as the adjustments are made to the fiducial values R_F. The open circle shows the result obtained when we set $R_F = R_{RSS}$, where R_{RSS} is the earlier ring radius scale derived from the radio-occultation experiment of *Voyager 1* (Simpson *et al.* 1983). NCP corrected this earlier radius scale through a readjustment to the radii, reducing the RSS radii by several kilometers, with the absolute value of the corrections increasing nonlinearly with radius. As a further test of the sensitivity to the radius scale, we applied a constant shift to the R_F. The solid point marked +5 shows the result when we increased R_F by 5 km everywhere, whereas the solid point marked −5 shows the result of a constant decrease of R_F by the same amount. If we were to optimize the solution by adjusting R_F, α_p, δ_p simultaneously, the pole would settle on a position far from either the NCP or Simpson pole. The +5 solution has $(\delta R)_{rms} = 2.0$ km, whereas the −5 solution has $(\delta R)_{rms} = 1.6$ km. These two trial solutions exhibit the sensitivity of our pole position to the fiducial radii, but neither solution indicates that such a revision to the NCP radial scale is actually called for. The NE paper addresses this point by fitting simultaneously to the Voyager data and to the 28 Sgr data set.

We conclude that the 28 Sgr standard data set is consistent with the NCP pole and radius scale obtained from analysis of *Voyager* data. In J2000.0 coordinates, the NCP values for the pole coordinates are

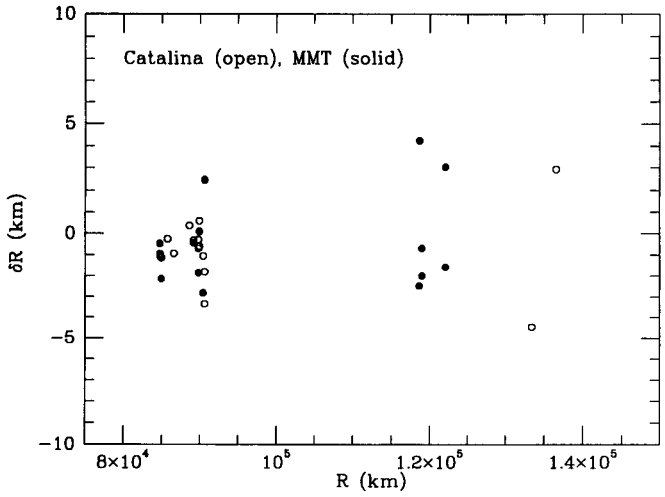

FIG. 13. Individual radial residuals at stations 1 and 2.

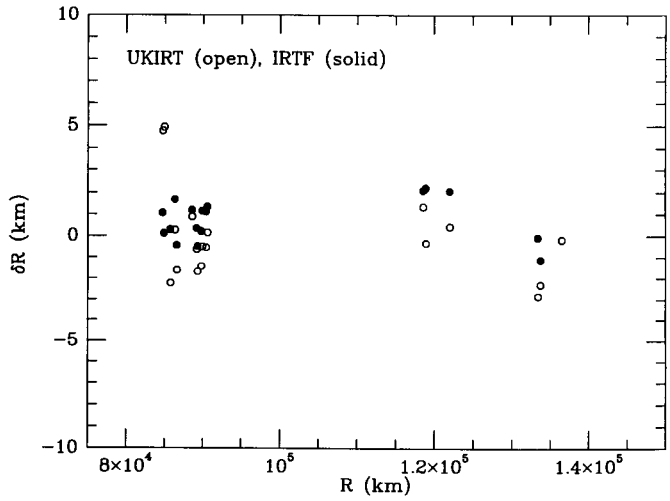

FIG. 15. Individual radial residuals at stations 5 and IRTF.

$$\alpha_p = 40.58850°,$$
$$\delta_p = 83.53824°. \quad (17)$$

Uncertainty in the pole coordinates from the 28 Sgr data is ±0.02° in α_p, and ±0.005° in δ_p, correlated with the error ellipse shown in Fig. 12.

It is useful to graphically examine the individual station residuals to assess the quality of the solution. Figure 13 shows residuals for stations 1 and 2, plotted as a function of ring radius R. The residuals are those tabulated in Table III and are with respect to the R_{NCP} and are calculated using the NCP pole, Eq. (17). The subsequent Figs. 14, 15, 16, and 17 show residuals for the remainder of the standard data set, including the NE timings for IRTF, Palomar, and McDonald. The residual plots for our best-fit solution with the pole position given by Eq. (16) are nearly indistinguishable. It is possible that some systematic timing differences may still exist in the standard data set, and elimination of some of the more discrepant data points may improve the fit. However, the principal conclusion that the 28 Sgr timings are concordant with the *Voyager* data is unlikely to change.

6. DISCUSSION

The 28 Sgr results presented here confirm the systematic reduction of the *Voyager* RSS ring radius scale by ~10 km and are consistent with a ring pole position deduced solely from *Voyager* data taken ~9 years earlier (NCP). In our analysis we would not expect to be sensi-

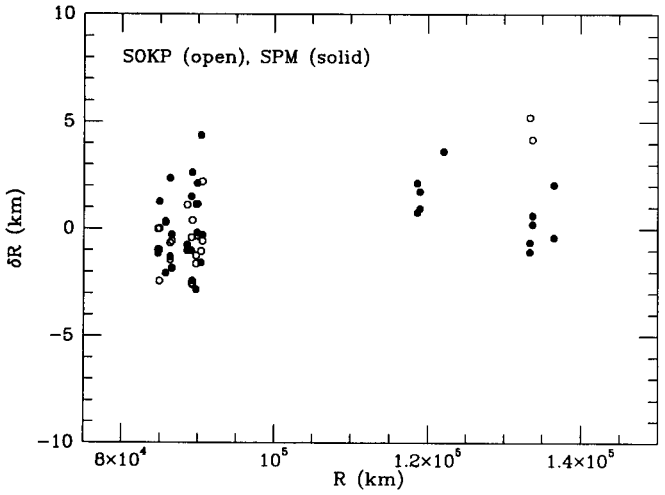

FIG. 14. Individual radial residuals at stations 3 and 4.

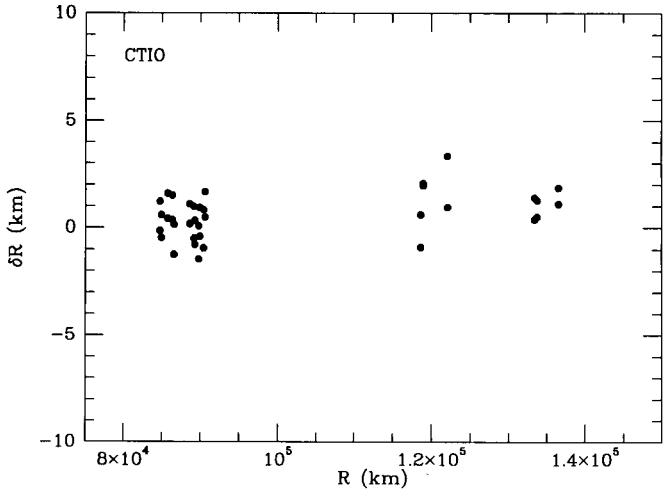

FIG. 16. Individual radial residuals at CTIO.

scribed below), and the model is then adjusted to improve

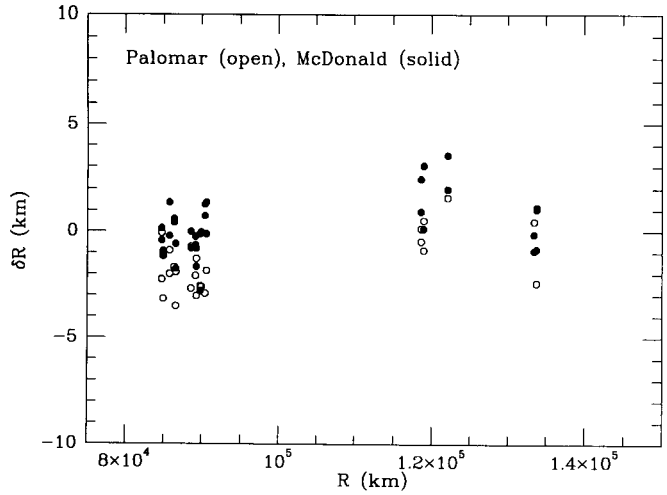

FIG. 17. Individual radial residuals at Palomar and McDonald.

tive to a possible change in the position of the ring pole (and consequently in the Saturn rotational pole) over the 8-year interval between the *Voyager* encounter and the 28 Sgr occultation for the following reasons.

The Sun-forced precession of a rotating oblate Saturn with a precession constant $H = (C - A)/C = 0.074$ (Hubbard and Marley 1989) would have a period of 7 million years, resulting in a polar motion less than 1 arcsec in 8 years, well below our detection limit. On similar grounds, we can rule out a "free precession" or the analog to the terrestrial Chandler wobble. The period of a Chandler-like wobble in Saturn's body frame would be $P_C \approx HP_S$, where P_S is Saturn's rotational period. We find $P_C = 6$ days. Seen from an inertial frame, this period would be $(A/C)P_S \sim 9.9$ hr, comparable to orbital periods within the rings. Since the rings would not respond as a unit to a changing Saturn pole position on such a short timescale, a Chandler-like wobble would not affect the pole of the ring plane. If Saturn were an inviscid ideal liquid planet, it may not wobble at all. Since Saturn is closer to the limit of an inviscid liquid than to a rigid body, rigid-body free precession can be neglected.

As shown in the NE paper, torques imposed on Saturn via precession of Titan's orbit can be larger than direct solar torques and can lead to a shorter precession period, although still not enough polar motion in 8 years to be important for our analysis. Although the total torque which is exerted on Saturn via its equatorial bulge can be readily calculated, the detailed response of Saturn, as a liquid body, to this torque remains to be investigated.

The analysis presented here is sensitive to differential distortions of fiducial ring features: i.e., the pole position derived from 28 Sgr data is quite sensitive to the assumption that all the fiducial features are coplanar, concentric circles. A collective oscillation of the fiducial features out of the mean ring plane, with a wavelength comparable to the radius of the rings and an amplitude of 11 km could lead to a pole position differing from the one found here by as much as 0.005°, the quoted uncertainty in δ_p. However, Nicholson *et al.* note that the influence of perturbing masses, such as the Sun and Saturn satellites, is very small and could only produce distortions out of the ring plane with amplitudes less than 200 m. A warping of this amplitude at the outer ring A would go completely unnoticed in our analysis.

ACKNOWLEDGMENTS

The CTIO observations would not have been possible without the work of the CTIO mountain electronics and observer support crew. D. Jewitt played a key role in obtaining the UKIRT data. E. Asphaug participated in some of the initial data analysis. B. Owen and S. Newhall of JPL kindly provided necessary ephemerides used in this work. R. French and P. Nicholson (NE) played a crucial role in helping us debug our reduction algorithms, in understanding instrumental effects in the time base, and in discussions leading to the final version of this paper. This work was supported by NASA Grants NAGW-1555 and NAGW-1876 and NSF Grant AST-8715373.

REFERENCES

BLANDFORD, R. D., AND R. NARAYAN 1992. Cosmological applications of gravitational lensing. *Annu. Rev. Astron. Astrophys.* **30,** 311–358.

CAMPBELL, J. K., AND J. ANDERSON 1989. Gravity field of the Saturnian system from *Pioneer* and *Voyager* tracking data. *Astron. J.* **97,** 1485–1495.

COLBECK, L. A. 1990. *Facilities Manual of the Cerro Tololo Inter-American Observatory.*

COOKE, M. L., P. D. NICHOLSON, AND M. R. SHOWALTER 1992. Keeler gap inner edge variation. *EOS (Suppl.)* **73,** 177.

CUZZI, J. N., AND J. D. SCARGLE 1985. Wavy edges suggest moonlet in Encke's gap. *Astrophys. J.* **292,** 276–290.

FRENCH, R. G., J. L. ELLIOT, B. SICARDY, P. NICHOLSON, AND K. MATTHEWS 1982. The upper atmosphere of Uranus: A critical test of isotropic turbulence models. *Icarus* **51,** 491–508.

FRENCH, R. G., P. D. NICHOLSON, M. L. COOKE, J. L. ELLIOT, K. MATTHEWS, O. PERKOVIĆ, E. TOLLESTRUP, P. HARVEY, N. J. CHANOVER, M. A. CLARK, E. W. DUNHAM, W. FORREST, J. HARRINGTON, J. PIPHER, A. BRAHIC, I. GRENIER, F. ROQUES, AND M. ARNDT 1993. Geometry of the Saturn system from the 3 July 1989 occultation of 28 Sgr and Voyager observations. *Icarus* **103,** 163–214.

HUBBARD, W. B., D. M. HUNTEN, H. J. REITSEMA, N. BROSCH, Y. NEVO, E. CARREIRA, F. ROSSI, AND L. H. WASSERMAN 1990a. Results for Titan's Atmosphere from its Occultation of 28 Sagittarii. *Nature* **343,** 353–355.

HUBBARD, W. B., C. PORCO, R. CLARK, E. TURTLE, V. HAEMMERLE, D. HUNTEN, G. RIEKE, M. RIEKE, J. HALLER, J. HOLBERG, L. LEBOFSKY, R. MARCIALIS, D. MCCARTHY, B. MCCLEOD, M. BUIE, J. ELIAS, D. JEWITT, E. PERSSON, T. BOROSON, S. WEST, R. LANDAU, AND L CARRASCO 1990b. Saturn's pole position and ring radius scale from 28 Sgr occultation. *Bull. Am. Astron. Soc.* **22,** 1041.

HUBBARD, W. B., AND M. S. MARLEY 1989. Optimized Jupiter, Saturn, and Uranus interior models. *Icarus* **78,** 102–118.

HUBBARD, W. B., P. D. NICHOLSON, E. LELLOUCH, B. SICARDY, A. BRAHIC, F. VILAS, P. BOUCHET, R. A. MCLAREN, R. L. MILLIS, L. H. WASSERMAN, J. H. ELIAS, K. MATTHEWS, J. D. MCGILL, AND C. PERRIER 1987. Oblateness, radius, and mean stratospheric temperature of Neptune from the 20 August 1985 occultation. *Icarus* **72,** 635–646.

HUBBARD, W. B., B. SICARDY, D. M. HUNTEN, A. BRAHIC, C. FERRARI, D. GAUTIER, J. LECACHEUX, E. LELLOUCH, F. ROQUES, J. E. ARLOT, F. COLAS, W. THUILLOT, F. SÈVRE, J. L. VIDAL, C. BLANCO, S. CRISTALDI, C. BUIL, A. KLOTZ, E. THOUVENOT, H. J. REITSEMA, N. BROSCH, Y. NEVO, E. CARREIRA, F. ROSSI, L. H. WASSERMAN, C. C. PORCO, R. V. YELLE, B. RIZK, W. BEISKER, M. NEZEL, B. RIEDEL, H. DENZAU, K. ZDANAVICIUS, K. CERNIS, M. HOFFMANN, E. H. GEYER, R. W. FORREST, I. K. M. NICOLSON, R. MILES, G. APPLEBY, F. M. FLASAR, D. TOUBLANC, AND G. CORUGEDO 1993. The occultation of 28 Sgr by Titan. *Astron. Astrophys.* **269,** 541–563.

LANDAU, R., G. GRASDALEN, AND G. C. SLOAN 1992. Three-beam chopping: An efficient infrared observing technique. *Astron. Astrophys.* **259,** 696–700.

NARAYAN, R., AND W. B. HUBBARD 1988. Theory of anisotropic refractive scintillation: application to stellar occultations by Neptune. *Astrophys. J.* **325,** 503–518.

NICHOLSON, P., AND C. PORCO 1988. A new constraint on Saturn's zonal gravity harmonics from *Voyager* observations of an eccentric ringlet. *J. Geophys. Res.* **93,** 10209–10224.

NICHOLSON, P. D., M. L. COOKE, AND E. PELTON 1990. An absolute radius scale for Saturn's rings. *Astron. J.* **100,** 1339–1362.

PORCO, C., P. D. NICHOLSON, N. BORDERIES, G. E. DANIELSON, P. GOLDREICH, J. B. HOLBERG, AND A. L. LANE 1984. The eccentric Saturn ringlets at $1.29R_S$ and $1.45R_S$. *Icarus* **60,** 1–16.

PORCO, C., AND P. D. NICHOLSON 1987. Eccentric features in Saturn's outer C ring. *Icarus* **72,** 437–467.

SICARDY, B., A. BRAHIC, C. FERRARI, D. GAUTIER, J. LECACHEUX, E. LELLOUCH, F. ROQUES, J. E. ARLOT, F. COLAS, W. THUILLOT, F. SÈVRE, J. L. VIDAL, C. BLANCO, S. CRISTALDI, C. BUIL, A. KLOTZ, AND E. THOUVENOT 1990. Probing Titan's atmosphere by stellar occultation. *Nature* **343,** 350–353.

SIMPSON, R. A., G. L. TYLER, AND J. B. HOLBERG 1983. Saturn's pole: Geometric correction based on *Voyager* UVS and radio occultations. *Astron. J.* **88,** 1531–1536.

TURTLE, E., C. PORCO, W. HUBBARD, V. HAEMMERLE, R. CLARK, D. HUNTEN, G. RIEKE, M. RIEKE, J. HALLER, J. HOLBERG, L. LEBOFSKY, R. MARCIALIS, D. MCCARTHY, B. MCLEOD, M. BUIE, J. ELIAS, D. JEWITT, E. PERSSON, T. BOROSON, S. WEST, R. LANDAU, AND L. CARRASCO 1990. The kinematics of Saturn's major narrow rings from combined *Voyager* and ground-based data. *Bull. Am. Astron. Soc.* **22,** 1041.

TURTLE, E., C. PORCO, V. HAEMMERLE, W. HUBBARD, AND R. CLARK 1991. The kinematics of eccentric features in Saturn's Cassini division from combined *Voyager* and ground-based data. *Bull. Am. Astron. Soc.* **23,** 1179.